13C ENDOR Spectroscopy of Lipoxygenase−Substrate Complexes Reveals the Structural Basis for C−H Activation by Tunneling

Masaki Horitani,[†,⊥,∞] Adam R. Offenbacher,[‡,⊥] Cody A. Marcus Carr,[‡,#] Tao Yu,[§] Veronika Hoeke,[†] George E. Cutsail III,[†,¶] Sharon Hammes-Schiffer,[§] Judith P. Klinman,[*,‡,||] and Brian M. Hoffman[*,†]

[†]Department of Chemistry, Northwestern University, Evanston, Illinois 60208, United States
[‡]Department of Chemistry and California Institute for Quantitative Biosciences (QB3), [||]Department of Molecular and Cell Biology, University of California, Berkeley, California 94720, United States
[§]Department of Chemistry, University of Illinois at Urbana−Champaign, Urbana, Illinois 61801, United States

Ⓢ *Supporting Information*

ABSTRACT: In enzymatic C−H activation by hydrogen tunneling, reduced barrier width is important for efficient hydrogen wave function overlap during catalysis. For native enzymes displaying nonadiabatic tunneling, the dominant reactive hydrogen donor−acceptor distance (DAD) is typically ca. 2.7 Å, considerably shorter than normal van der Waals distances. Without a ground state substrate-bound structure for the prototypical nonadiabatic tunneling system, soybean lipoxygenase (SLO), it has remained unclear whether the requisite close tunneling distance occurs through an unusual ground state active site arrangement or by thermally sampling conformational substates. Herein, we introduce Mn^{2+} as a spin-probe surrogate for the SLO Fe ion; X-ray diffraction shows Mn-SLO is structurally faithful to the native enzyme. 13C ENDOR then reveals the locations of 13C10 and reactive 13C11 of linoleic acid relative to the metal; 1H ENDOR and molecular dynamics simulations of the fully solvated SLO model using ENDOR-derived restraints give additional metrical information. The resulting three-dimensional representation of the SLO active site ground state contains a reactive (a) conformer with hydrogen DAD of ∼3.1 Å, approximately van der Waals contact, plus an inactive (b) conformer with even longer DAD, establishing that stochastic conformational sampling is required to achieve reactive tunneling geometries. Tunneling-impaired SLO variants show increased DADs and variations in substrate positioning and rigidity, confirming previous kinetic and theoretical predictions of such behavior. Overall, this investigation highlights the (i) predictive power of nonadiabatic quantum treatments of proton-coupled electron transfer in SLO and (ii) sensitivity of ENDOR probes to test, detect, and corroborate kinetically predicted trends in active site reactivity and to reveal unexpected features of active site architecture.
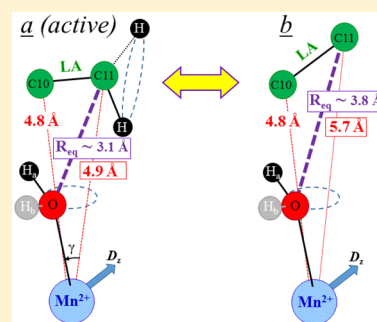
INTRODUCTION

Among the many remarkable properties of naturally occurring enzymes is their ability to achieve enormous accelerations of chemical reactions, upward of 10^{26}-fold,[1] over their solution counterparts. Because these enhanced rates occur under "green" conditions (i.e., atmospheric pressure, room temperature, and aqueous solutions), the computational design (de novo) and re-engineering of enzymes to perform biologically inaccessible chemical transformations has emerged as an active area of biochemical and bioengineering research with immediate industrial and pharmaceutical implications.[2−4] While electrostatics are expected to contribute significantly to the rate of enzymatic reactions,[5,6] the inability to match nature's rate enhancements in computational (rational) design practices (even with assistance from directed evolution)[7−9] underscores the current ineffectiveness in the application of mainstream concepts to our full understanding of the origins of enzyme catalysis.

Enzymatic C−H activation has played a central role in the emerging idea that active sites must undergo transient compaction (or compression) for efficient catalysis.[10−13] This concept has been further recognized in methyl (group) transfer, suggesting a broader generality for active site compaction in enzyme catalysis.[14,15] The hydrogen transfer mechanism of C−H activation is most generally described by a quantum tunneling model,[16] in which both protium and its heavier isotopes penetrate a barrier along the transferring nuclear coordinate. In such instances, the corresponding nuclear transfer distance will approximate the de Broglie wavelength for the respective isotope (ca. 0.7 Å for proton and 0.5 Å for deuterium), introducing the requirement for protein motions that can bring the H-donor and acceptor within an effective tunneling distance of ca. 2.7 Å in native enzymes.[17]

Native soybean lipoxygenase-1 (SLO) has presented some of the most compelling kinetic evidence for the quantum tunneling model, from observations of a greatly inflated, nearly temperature independent kinetic isotope effect on a single, rate-

determining step (Scheme 1) near room temperature.[18] These kinetic properties of SLO have been successfully reproduced

Scheme 1. SLO Catalyzes the Transfer of a Hydrogen Atom from Donor Carbon 11 (C11) of LA to a Mononuclear, Non-Heme Ferric Hydroxide Reactive Center[a]
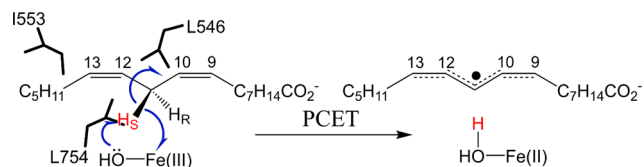
[a]Hydrogen abstraction from the pro-S position on C11 is mediated by a proton-coupled electron transfer reaction (PCET),[48,75] in which the metal-bound hydroxide accepts the proton and iron accepts the electron. The putative positioning of residues discussed in the text (I553, L546, and L754) is shown for reference.

using nonadiabatic models in which the isotope dependence of the rate constant is strongly influenced by the equilibrium proton donor–acceptor distance and motions, which in turn may be affected by the protein structure and thermal motions.[19−22] Although many atomic resolution X-ray crystal structures have been reported for SLO (for examples, see refs 23−25), efforts over several decades to solve the structure of an enzyme–substrate (ES) complex (with either the natural substrate linoleic acid (LA) or a substrate analogue) have been unsuccessful. This may be the consequence of a restricted substrate access portal and binding site as seen in crystal forms of SLO.[26] We note that a crystal structure of the enzyme–product of the L-3 isoenzyme of soybean lipoxygenase has been reported,[27] but the orientation of the substrate and product within the active site may be different.[28] While this enzyme–product structure can provide insights into the mode of fatty acid binding, our understanding of catalytic C−H cleavage remains hindered by the lack of structural information regarding the dominant ES complex.

To overcome the inability to crystallize the substrate complexes of SLO, we have instead exploited high-precision electron–nuclear double resonance (ENDOR) spectroscopy, which has become a central tool for determining the coordination environment of biological metal centers, in particular the active sites of enzyme intermediates.[29,30] ENDOR (and related ESEEM/HYSCORE) spectroscopies provide NMR spectra of nuclei that interact with the electron spin of a paramagnetic center through the electron–nuclear hyperfine interaction. Although ENDOR is most commonly used to characterize the coordination sphere of biological metal ions by interrogating nuclei involved in covalent through-bond interactions with the paramagnetic center, this technique can also give high-precision structural information for atoms in the active site that are in close proximity to the metal ion but not covalently linked to it. Such nuclei exhibit a nonlocal, through-space dipolar coupling to the electron spin, the dipolar interaction matrix, $\mathbf{T}$, whose characterization yields the coordinates of those atoms relative to the metal site, thus directly providing metrical information about the active site architecture.[31,32]

The obvious application of this approach to a non-heme Fe enzyme like SLO is to use the Fe(NO) $S = 3/2$ state as a spin probe that is amenable to ENDOR measurements giving the distance between the Fe(NO) and substrate.[31,33] Unfortu-

nately, this is inapplicable for the SLO enzyme–substrate complex. An earlier EPR examination of SLO showed that the substrate LA and NO compete for active site occupancy,[34] and when LA and NO were added to SLO, there was no detectable Fe(NO) signal. We therefore turned to the $S = 5/2$ Mn^{2+} ion as a spin-probe surrogate for the iron cofactor of SLO to determine the distances and orientations of key ^{13}C atoms on LA relative to the metal site in SLO, having first shown by X-ray diffraction that Mn-SLO is structurally faithful to the native enzyme. Although there have been numerous advanced paramagnetic resonance studies of ligands coordinated to a Mn^{2+} ion,[35−41] to our knowledge this is the first application of Mn^{2+} ion as a spin-probe for determining the location of a nearby, noncoordinated substrate. As described, the characteristics of this high-spin Mn^{2+} ion make it extraordinarily advantageous in this role, although its use required the development of a new approach to the analysis of frozen-solution ENDOR spectra.

35 GHz pulsed ENDOR measurements yield the distances and orientations of $^{13}C10$ and the reactive $^{13}C11$ of LA relative to the metal site, while ^1H ENDOR of the metal-bound water ligand, in conjunction with molecular dynamics (MD) simulations using the experimental ENDOR-derived distances as restraints, yields their orientations. The resulting three-dimensional representation of the SLO active site equilibrium ground state contains a reactive enzyme conformer in which the elusive donor–acceptor distance (DAD) between C11 of LA and the metal-bound water is too long to permit efficient tunneling of hydrogen from donor to acceptor in the wild-type (WT) enzyme, as well as an inactive conformer where the DAD is even longer. This result provides compelling support that a key catalytic role of heavy atom thermal motions of the protein–ligand complex is to access configurations that allow effective hydrogenic wave function overlap during the course of C−H bond cleavage.

In addition, we present an ENDOR-based characterization of the ES structures of two previously studied active site mutants of SLO, the I553G variant and the L546A/L754A double mutant (DM); Figure 1A visualizes the positions of the mutated residues relative to the metal ion in the crystal
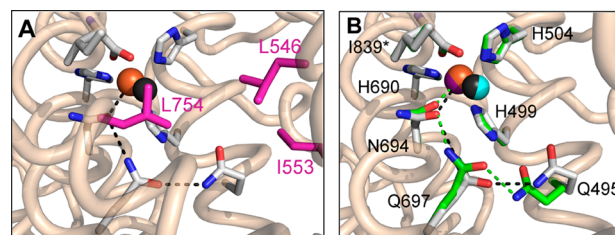
Figure 1. Active site of native Fe-SLO (1.4 Å; PDB: 3PZW) showing residues subject to mutation in this study (pink) (A) and structural comparison of first and second coordination spheres in crystal structures of native Fe-SLO and Mn-SLO (1.14 Å; PDB: 4WFO) (B). The structural overlay represents Mn-SLO (side chain carbons, green sticks; cofactor Mn−O(H_2) atoms, purple and dark gray spheres) and Fe-SLO (side chain carbons, gray sticks; cofactor Fe−O(H_2) atoms, orange and cyan spheres). Represented side chain oxygen and nitrogen atoms are colored red and blue, respectively. The explicitly shown side chains are labeled; the asterisk for I839 represents the terminal carboxyl group that ligates the metal cluster. A putative H-bond network[24,45] is designated by dashed lines. A comparative list of all metal–ligand distances is presented in Table S2.

structure of the substrate-free enzyme. Literature interpretations of extensive kinetic and theoretical studies have predicted a longer DAD in both of these SLO variants.[21,22,25,42] The current results show a clear elongation of the ground state equilibrium DAD (R_{eq}), validating the previous interpretations and highlighting the sensitivity of our ENDOR approach for detecting small changes to the heavy atom DAD. This report thus both provides a foundation for and confirmation of the theoretical analyses of the enzymatic C−H bond cleavage and introduces an important and timely physical methodology that has been hitherto lacking in the field.[10]

■ RESULTS

Kinetic and Structural Characterization of Mn-SLO. ENDOR studies on "rhombic" high-spin Fe(III) ($S = 5/2$) are unproductive because of rapid electron-spin relaxation. The resting ferrous form (integer spin, $S = 2$) of SLO is EPR silent,[34] and, as noted above, the traditional use of the Fe(NO) $S = 3/2$ system[31] as a spin probe also was unsuccessful. In agreement with earlier work,[34] when LA and NO were added to SLO, there was no detectable Fe(NO) signal. We thus turned to the $S = 5/2$ Mn^{2+} ion as a spin-probe substitute for Fe. The structural similarity observed between lipoxygenases with M^{2+} and M^{3+} at the active center (see refs 43−45 and references within) suggested that Mn-SLO would be a suitable structural surrogate. Moreover, although all characterized animal, plant, and prokaryotic lipoxygenases utilize iron as their active site cofactor, an emerging group of fungal lipoxygenases have been found to harbor a reactive manganese ion (designated henceforth as MnLOX).[46]

We present a biosynthetic approach to substitute the iron center in SLO for manganese (notated as Mn-SLO; see Materials and Methods for details). As isolated, WT Mn-SLO protein contains 0.9 ± 0.1 Mn and 0.03 ± 0.02 Fe per monomer. While fungal MnLOX enzymes have first-order rate constants (i.e., k_{cat}) of ∼10% relative to WT SLO (Table S1), the manganese form of SLO exhibits only 2−3% activity compared to that of Fe-SLO, which correlates with the amount of residual iron in our sample preparations. These data are consistent with the expectation that manganese-substituted iron lipoxygenases would be inactive.[47]

An X-ray structural analysis of Mn-SLO was performed, yielding a high-resolution structure (1.14 Å) (PDB: 4WFO), which is the first reported model of a manganese-substituted iron lipoxygenase. The global structure is practically superimposable (RMSD ∼ 0.3 Å) on the 1.4 Å model of WT Fe-SLO (PDB: 3PZW). The first sphere iron coordination sites of Mn-SLO and Fe-SLO are very similar (RMSD = 0.17 Å with regard to both metal and ligands; Figure 1B), with the notable exception of the shortening of the bond to the axial Asn694, from 2.9 Å in native SLO to 2.3 Å in Mn-SLO (Table S2); this translates to a change from five- to six-coordinate iron, which remains consistent with a hydrogen-bonding network that includes residues Q697 and Q495.[23,43] All other metal−ligand distances within the Mn-SLO coordination site are nearly identical to those for Fe-SLO (Table S2). The coordination number for the iron center in native SLO has been studied extensively and found to vary from five-coordinate in X-ray studies, where the iron center is likely to have undergone reduction by the X-ray beam, to a 40:60 mixture of a five-coordinate (5C) and six-coordinate (6C) site for the Fe^{2+} state of the enzyme in solution.[43] Early DFT calculations were unable to reproduce a 5C ligation unless a protein structural

constraint was imposed.[48] More recent QM/MM calculations identify two local minima,[45,49] one with a 5C and another with a 6C Fe center, consistent with the experimental observations of a 40:60 mixture, respectively, in solution for WT Fe^{2+}-SLO. The most recent computational study shows that the hydrogen-bonding network composed of residues Q697 and Q495, as well as N694, is maintained in both the 5C and 6C structures.[45] Overall, the X-ray structure of Mn-SLO and its comparison to WT SLO makes it clear that Mn substitution provides a faithful structural analogue to native SLO.

EPR Spectra of Mn-SLO. *EPR of WT Mn-SLO.* The absorption-display EPR spectra collected from natural-abundance LA complexes of Mn-SLO by continuous-wave (CW) "rapid passage" methods at 2 K or by the echo-detected EPR technique (Figure 2A and S1A) are characteristic of an $S =$
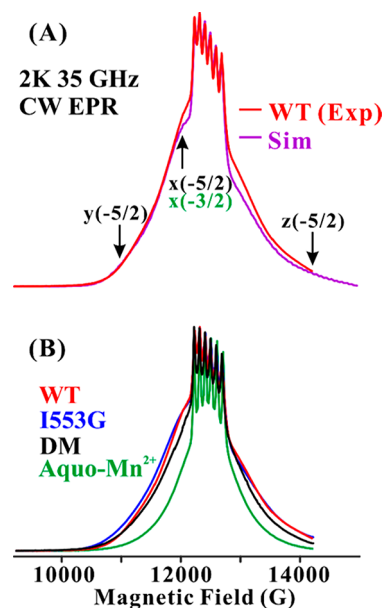
Figure 2. (A) 35 GHz CW rapid-passage EPR spectrum (red) and simulation (purple) for Mn-SLO WT with LA at 2 K. Conditions: microwave frequency ∼ 34.98 GHz, microwave power = 1 mW, 100 kHz field modulation amplitude = 0.7 G, and $T = 2$ K. Simulation parameters are listed in Table 1. (B) Comparison of 35 GHz CW rapid-passage EPR spectra for Mn-SLO with LA (WT; red, I553G; blue, DM; black) and $[Mn^{2+}(H_2O)_6]$ (green). Conditions: same as those in A. Simulations for mutants are in Figure S2; ZFS parameters are in Table 1.

5/2 ion with small zero-field splitting (ZFS), with the principal ZFS parameter, D, much less than the microwave quantum ($h\nu$).[50] Such spectra show a central ^{55}Mn ($I = 5/2$) sextet arising from hyperfine interactions, $A \sim 91$ G, that is associated with transitions between the $m_s = +1/2$ and $−1/2$ electron-spin substates. These features "ride on" and are flanked by significantly broader signals from the four "satellite" transitions involving the other electron-spin substates ($m_s \pm 5/2 \Leftrightarrow \pm 3/2$; $\pm 3/2 \Leftrightarrow \pm 1/2$). The net absorption spectrum is the sum of the five envelopes of these five transitions among substates, each of which has a well-defined shape and is spread over a range of fields that is defined by the m_s values for the envelope and the magnitudes of the ZFS parameters; the contribution of each envelope is weighted by the thermal population of the contributing m_s levels.[51] The overall breadth of the pattern is proportional to the magnitude of D, which in turn increases

with deviations of the coordination sphere of the Mn^{2+} ion from spherical symmetry; details of the shape of the pattern are determined by the rhombicity parameter, $0 \le \lambda \le 1/3$, whose value increases with deviations from axial symmetry around the principal ZFS axis ($\lambda = 0$).[52] The 2 K EPR spectra (Figure 2B and S1A) of WT Mn-SLO with LA substrate are only slightly broader than that of the simple aquo-Mn^{2+} ion, indicating that the ZFS parameter for Mn-SLO is only slightly larger. Table 1 compiles the parameters [D, λ] obtained by simulations of the Mn-SLO samples studied here.

Table 1. ZFS Parameters of Mn^{2+} in Mn-SLO[a]

	D (MHz)	λ	f
WT	+1320	0.17	0.32
I553G	+1420	0.16	0.32
DM	+1250	0.20	0.36
MnLOX[b]	+2100 to +3000	0.13−0.23	N.R.

[a]D is the axial ZFS parameter, λ is the rhombicity (E/D), and f represents the breadth of Gaussian distributions in D and E employed in the simulations, each with a width that is the fraction f times the parameter (see the Supporting Information). [b]Native manganese lipoxygenase from fungus; values are reported from ref 53; N.R. = not reported.

In describing the ENDOR measurements, it is important to note that conventional derivative-display spectra miss 80% of the full Mn^{2+} spectrum. They typically show only the classic ^{55}Mn hyperfine-split sextet associated with the $|m_s| = 1/2$ sublevels (Figure S1B) and are equivalent to that of an $S = 1/2$ center with isotropic g-tensor and hyperfine splitting. The signals from the other four satellite transitions, which generate the "wings" of the absorption-display spectra of Figures 2 and S1A, are, at most, only barely detectable.

Interestingly, comparison of EPR spectra of Mn-SLO with the Mn^{2+} ion site of the native manganese lipoxygenase, MnLOX,[53] suggests that the active site of the latter is not identical to that of Mn-SLO, as the axial ZFS parameter of MnLOX, although still small, is distinctly greater ($D \sim +2100$ to +3000 MHz) (Table 1). The larger ZFS for MnLOX is consistent with a greater asymmetry of its metal coordination and larger metal B-factors relative to Mn-SLO, consistent with cryogenic X-ray crystal structures.[54]

EPR of I553G and DM Mn-SLO. The site of mutation corresponding to I553G is remote from the metal ion (Figure 1A), and as might be anticipated, this variant does not perturb the coordination sphere of the Mn^{2+} ion: the variant EPR spectrum ($D = +1420$ MHz, $\lambda = 0.16$) is essentially the same as that of the WT enzyme ($D = +1320$ MHz) (Figures 2B, S1, and S2 and Table 1). The L754A mutation of the L546A, L754A mutation pair in the DM Mn-SLO variant is closer to the metal ion (Figure 1A), but in complex with LA this variant's EPR spectrum likewise is essentially equivalent ($D = +1250$ MHz, $\lambda = 0.20$) to that of the WT enzyme complex (Figures 2B, S1, and S2 and Table 1). The 35 GHz Davies pulsed ENDOR spectra from ^1H of bound H_2O and ^{14}N of bound histidines collected for the WT and mutant enzymes (Figure S3) confirm that the residue changes indeed have negligible influence on the coordination sphere of the Mn^{2+} ion itself.

ENDOR of a Mn^{2+} ($S = 5/2$) Center. For a single molecular orientation of a paramagnetic center of spin S, the first-order ENDOR spectrum for an $I = 1/2$ nucleus (^{13}C, ^1H) obtained by monitoring an EPR transition between adjacent substates, m_s

$\Leftrightarrow m_s + 1$ comprises a signal from each of the substates. For this study, the two frequencies are conveniently written as offsets ($\delta\nu_{ms}$) from the nuclear Larmor frequency, ν_N

$$\delta\nu_{ms} = \nu_{ms} - \nu_N = m_s A \quad m_s = -S, -S + 1, ..., S - 1 \tag{1}$$

$$\delta\nu_{ms+1} = \nu_{ms+1} - \nu_N = (m_s + 1)A$$

where A is the orientation-dependent electron–nuclear hyperfine coupling interaction.

Hyperfine Interactions and $S = 5/2$. The hyperfine interaction between the Mn^{2+} ion of SLO and the ^{13}C of LA as observed here is overwhelmingly dominated by the coupling that arises from the through-space electron–nuclear dipolar interaction. We have shown previously that precise locations of active site, but noncoordinated, nuclei can be determined by ENDOR measurements of the axial dipolar interaction matrix, **T** (eq 2).[31] Although the Mn^{2+} spin is partially delocalized over its ligands, in the Supporting Information we show that, at the Mn−^{13}C distances being interrogated here, the three principal components of this interaction matrix in its principal axis coordinate frame can be written as a point dipole interaction with spin on Mn^{2+} alone, characterized by the ^{13}C dipolar parameter, T

$$\mathbf{T} = [-T, -T, 2T] \quad T = \frac{20\rho_{eff}}{r^3}(\text{MHz}) \tag{2}$$

where r (Å) is the Mn−^{13}C distance, and the large positive principal value (2T) lies along the Mn−^{13}C vector. As described in the Supporting Information, an appropriately chosen value for an effective spin density on the metal ion, ρ_{eff}, makes this point-dipole formulation of eq 2 precisely equal to the sum over the dipolar interactions between ^{13}C and the spin density as distributed over the Mn^{2+} ion and its ligands. This conclusion is based on a combination of DFT computations of the spin distribution in the SLO Mn^{2+} coordination sphere with model dipolar-interaction calculations that incorporate the spin distribution. The analysis indicates that interpretation of the observed couplings with eq 2 yields the correct Mn−^{13}C distances when ρ_{eff} is essentially unity ($\rho_{eff} = 0.994$). We emphasize that in the Supporting Information we present a detailed analysis of the uncertainties in the distances determined from the ENDOR determinations of T; this analysis confirms conclusions based on distances so obtained and reported below.

In addition to the dipolar interaction, even at such great Mn−^{13}C distances we observe so-called Pauli delocalization through polarization of closed shells.[55] This induces a tiny spin density at carbon ($\sim10^{-5}$−10^{-6} of an electron spin), thereby generating a small isotropic ^{13}C hyperfine coupling, denoted a_{iso}.[56] As a result the measured hyperfine interaction is a matrix, A, that is a sum of the two interactions

$$A = a_{iso} \cdot 1 + \mathbf{T} \tag{3}$$

A key benefit of using ENDOR to measure distances from nearby nuclei to an $S = 5/2$ Mn^{2+} ion like that in SLO, which is in the regime where $D \ll h\nu$ (microwave energy), is that for a given orientation of the external field relative to the molecular frame the effective hyperfine offset from ν_N for each $|m_s|$ is given by the intrinsic value of the coupling, A, multiplied by $|m_s|$, eq 1. Thus, whereas the ENDOR offsets in the response for the $|m_s| = 1/2$ sublevels are the same as would be seen for an $S = 1/2$ center, the offsets for the $|m_s| = 3/2, 5/2$ doublets are 3

and 5 times greater, respectively. This multiplicative effect for the hyperfine frequencies of nuclei coupled to an $S = 5/2$ Mn^{2+} ion sharply extends the "horizon" to which an ENDOR measurement can characterize the dipolar interaction component and, through this, calculate the distance to a substrate nucleus and the orientation of the Mn-nuclear vector. Consider a Mn^{2+} ion center whose ENDOR spectra can resolve a dipolar hyperfine interaction, $A = T$ (eq 2), down to a minimum resolvable offset, $\delta\nu_{min}$ (eq 1). According to eq 2, in this case the horizon for measuring a Mn-^{13}C distance, denoted r_{max}, expands with $|m_s|$, eq 4

$$r_{max}(m_s) = \left[\frac{|m_s|20}{\delta\nu_{min}}\right]^{1/3} \qquad (4)$$

($\delta\nu_{min}$, MHz; r_{max}, Å). Thus, for an $S = 5/2$ ion, the farthest horizon is associated with the $|m_s| = 5/2$ sublevels, and the distance from Mn to the horizon is nearly double that provided by an $S = 1/2$ center (only $|m_s| = 1/2$ sublevels)

$$r_{max}(|5/2|) = (5)^{1/3}r_{max}(|1/2|) = 1.71r_{max}(|1/2|) \qquad (5)$$

In fact, as will be seen, the resulting horizon for a ^{13}C in SLO is no less than ~6 Å.

*Orientation Selection and Determination of **A***. For analysis of the ENDOR spectra of this study, it is important to understand in some detail the low-temperature, frozen-solution ("powder") EPR spectra of a randomly oriented $S = 5/2$ center, in particular the implications for ENDOR measurements made at fields across the *entire* EPR envelope. Figure 3, top, shows idealized absorption EPR simulations for an $S = 5/2$ system with small ZFS ($D = +1250$ MHz, $\lambda = 0.2$) at room temperature, omitting the ^{55}Mn ($I = 5/2$) hyperfine splitting. As noted above, the spectrum is the sum of intensities associated with five sets of transitions: those between the $m_s = \pm 1/2$ substates, plus the four "satellite" transitions: $\pm 5/2 \Leftrightarrow \pm 3/2$; $\pm 3/2 \Leftrightarrow \pm 1/2$. In reality, each orientation of the Mn^{2+} center exhibits hyperfine splitting by the essentially isotropic hyperfine coupling to ^{55}Mn ($I = 5/2$), $A \sim 91$ G, and as illustrated in Figure 3, middle, this generates the hyperfine pattern seen for the $m_s = \pm 1/2$ envelope and broadens the other envelopes by ~450 G.

At each value of the external magnetic field, the EPR intensity for a $m_s \Leftrightarrow m_s - 1$ satellite EPR envelope corresponds to a well-defined subset of orientations of the field relative to the ZFS tensor axes. As shown in Figure 3, top, the extremes of the signal for each such envelope are associated with orientations where the external field lies along the principal axes with the smallest (y) and largest (z) ZFS splittings; the features of maximum intensity are associated with orientations that exhibit the intermediate ZFS principal value, x. A 2D field-frequency pattern of the resulting orientation-selective ENDOR spectra collected at fields across any one of these envelopes in principle could be analyzed to yield a hyperfine tensor, in precise analogy to the protocol we devised for ENDOR analysis of 2D field-frequency patterns of ENDOR responses collected across the EPR envelope of an $S = 1/2$ center.[57−59]

Unfortunately, as shown in Figure 3, top and middle, at "high" temperatures, $T \gg D/k$, both edges of the summed EPR envelope for this $S = 5/2$ center are equivalent single-crystal-like fields that are associated only with the field along the (z) axis of ZFS tensor, while the intensity of the EPR spectrum of this $S = 5/2$ center at any arbitrary field value is the sum of the contributions from as many as all four of the satellite envelopes
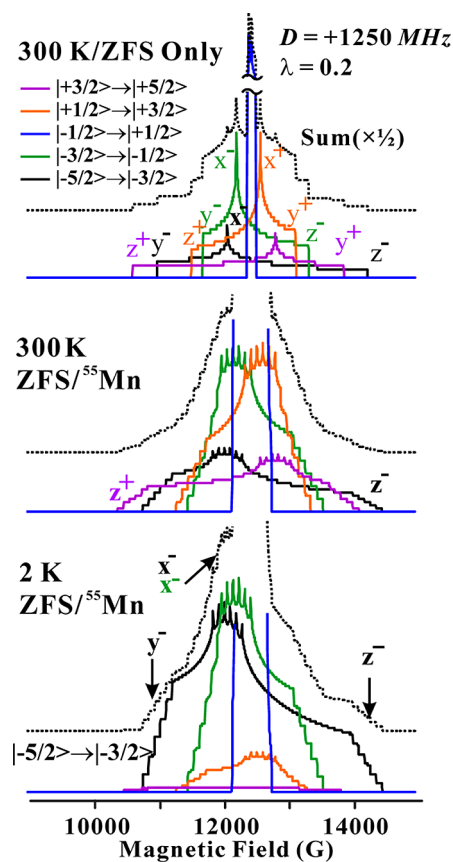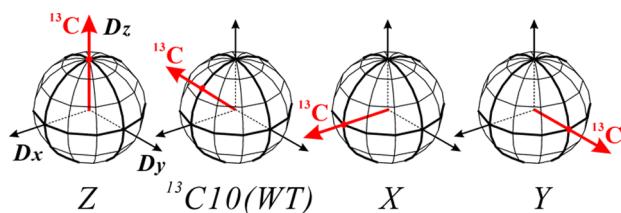

Figure 3. Idealized EPR absorption spectra. The absorption EPR simulations with no EPR line width for the high-spin $S = 5/2$ system with small zero-field splitting at 300 K (top), 300 K with ^{55}Mn hyperfine (middle), and 2 K with ^{55}Mn hyperfine (bottom). Simulated ZFS parameters are $D = +1250$ MHz and $\lambda = 0.2$. Individual transitions are differentiated by colored lines, as indicated. The sum of individual simulations is shown as a black dotted line, and its intensity is multiplied by (1/2). The principal axes of ZFS are also indicated.

(which exhibit orientation-selective ENDOR spectra) plus the central envelope (which yields a "powder" ENDOR spectrum, the sum of responses from all orientations). The resulting ENDOR spectrum collected from such a summed EPR spectrum represents too many distinct orientation-selective responses to be analyzable; furthermore, even for samples prepared with singly ^{13}C-labeled LA, there can be responses from multiple conformations of the substrate (see sections below). The result is that the 2D ENDOR pattern for such a high-temperature $S = 5/2$ spin system in general defies orientation-selective analysis.

However, the higher-lying m_s levels are thermally depopulated at 2 K, and as seen in Figure 3, bottom, this greatly simplifies the EPR spectrum and thus orientation-selective ENDOR spectra. This feature restores our ability to analyze orientation selectivity in the ENDOR responses, enabling determination of hyperfine coupling tensors. Although, as shown in Figure 3, bottom, the center of the 2 K EPR spectrum is dominated by the $m_s = \pm 1/2$ envelope with its "powder" ENDOR spectrum, the thermal depopulation leaves the extreme "wings" of the low-temperature spectrum as "single-crystal-like" EPR responses from the $m_s = -5/2 \Leftrightarrow -3/2$ envelope alone: when the external field is set to the low-field edge, it selects orientations where the field is along the ZFS y-axis; when it is set to the high-field edge, the field is along the

ZFS *z*-axis. Thus, these edges give simple "single-crystal-like" ENDOR responses associated with the *y* and *z* ZFS orientations. Away from the edges of the 2 K EPR signal, the $m_s = -5/2 \Leftrightarrow -3/2$ envelope still dominates the spectrum, although there is in addition a distinguishable contribution from $m_s = -3/2 \Leftrightarrow -1/2$; the $m_s = +1/2 \Leftrightarrow +3/2$ envelope contributes only minimally, and the $m_s = +3/2 \Leftrightarrow +5/2$ envelope is completely suppressed.
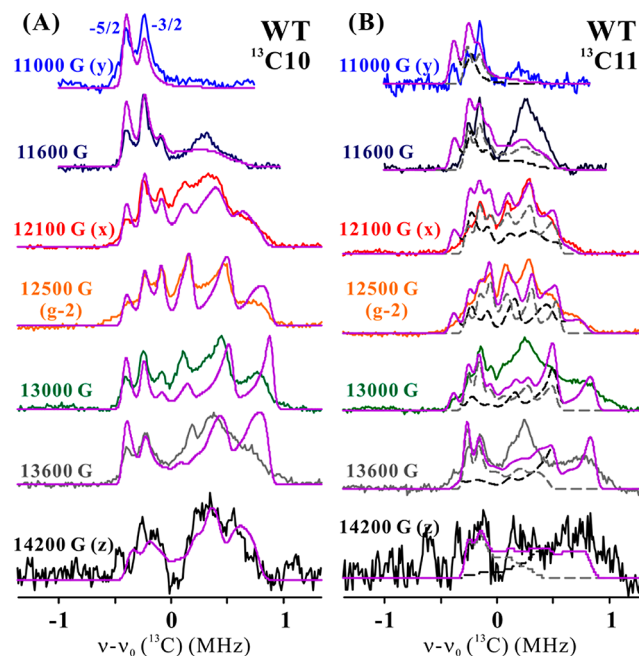
This simplification of the EPR and ENDOR spectra through thermal depopulation of electron spin substates enables determination of the hyperfine tensor of a ^{13}C label in LA, *A*, through a "multipass", 2D data-collection/analysis protocol that involves iterative combination of single-crystal-like ENDOR spectra and 2D field-frequency patterns of ^{13}C ENDOR spectra taken across the EPR envelope of the Mn^{2+} ion and enables precise determination of hyperfine tensors. To begin the analysis, we examine the behavior of the high- and low-frequency edges of the ENDOR spectra as the field of observation traverses the EPR envelope, to obtain approximate values for the maximum and minimum hyperfine shifts. Next, as illustrated in Figure S4, inspection of the single-crystal-like ENDOR spectra collected at the high and low-field edges of the EPR spectrum, plus a spectrum collected at $g \sim 2$, gives a preliminary value for *T* and also a rough indication of the orientation of the $Mn-^{13}C/^1H$ vectors relative to the ZFS axes, identifying a nearest "canonical" orientation as schematized in Figure 4. Finally, a full 2D pattern, as exemplified by the

Figure 5. 35 GHz 2D field-frequency pattern ^{13}C Mims ENDOR for Mn-SLO WT with $^{13}C10$-LA (A) and $^{13}C11$-LA (B) and simulation (purple) at 2 K. Conditions: microwave frequency ~ 34.8 GHz, MW pulse length $(\pi/2)$ = 30 ns, τ = 500 ns, repetition rate =100 Hz, and temperature of 2 K. Simulation parameters are listed in Table 2.

Figure 4. The three "canonical" orientations of the $Mn-^{13}C$ vector relative to the ZFS *x*, *y*, and *z* axes, along with the orientation determined experimentally ($^{13}C10$(WT)), with the vector in the *x*–*z* plane, rotated by an angle, θ = 50° away from *z*.

patterns for $^{13}C10$ and $^{13}C11$ of LA bound to WT-SLO, Figure 5, and mutants, S5 and S6, is then simulated, in a process that starts with parameters derived from the preliminary rough analyses, to yield the full hyperfine tensor, giving both accurate values for any isotropic term and for the axial dipolar contribution, **T**, eq 2, plus a precise orientation of **T** relative to the ZFS tensor axes. The unique direction of **T** (eq 2) corresponds to the direction of the $Mn-^{13}C$ vector relative to the ZFS axes, as shown for $^{13}C10$ of LA in WT enzyme in Figure 4.

ENDOR of WT Mn-SLO. ^{13}C *ENDOR of LA Substrate.* We collected 2 K 2D patterns of ^{13}C ENDOR spectra taken across the EPR envelope of the Mn^{2+} ion of WT Mn-SLO with $^{13}C10$- and $^{13}C11$-LA noncovalently bound in the enzyme active site, Figure 5. The optimized simulations of these patterns shown in Figure 5 yield the hyperfine tensors for the $^{13}C10$- and $^{13}C11$-LA complexes of Mn-SLO (Table 2). For both $^{13}C10$ and $^{13}C11$, the Mn–C vectors, and thus the C10–C11 fragment of the LA chain, lie essentially in the *x*–*z* plane of the ZFS tensor (Table 2; see Figures 4, S4, bottom). As a consequence of the simplification provided by this orientation, ENDOR spectra collected for all labels at the low-field edge of the EPR

spectrum, Figure 6, provide high-resolution single-crystal-like ENDOR responses that not only directly give precise values of $A_y = A_\perp$, and thus the Mn–C distance through eq 2, but also provide sufficiently high resolution to detect, in some cases, the contribution of minority conformational substates whose presence is masked in the majority of the 2D patterns.

$^{13}C10$-LA. The orientation of the Mn–C10 vector within the *x*–*z* plane of the ZFS tensor ($\phi \sim 0$, Table 2, Figures 4 and S4), together with the exceptionally high resolution of ENDOR spectra collected at the low-field edge of the EPR spectrum, Figure 6, yield low-field single-crystal-like ENDOR spectra with two peaks associated with the $m_s = -5/2 \Leftrightarrow -3/2$ EPR transition, with single-crystal-like frequency offsets arising for the magnetic field perpendicular to the Mn–$^{13}C10$ vector, $\delta\nu(m_s) = m_s A_\perp$, where $m_s = -5/2, -3/2$. This high resolution allows a precise refinement of the value for $A_\perp$ determined from the 2D pattern. Interestingly, the simulations, as confirmed by the low-field spectrum, show that $A_\parallel \neq 2A_\perp$ for $^{13}C10$. As a result, the simulations yield not only the Mn–$^{13}C10$ dipolar coupling strength, *T* = 0.175 MHz, corresponding through eq 2 to the Mn–C distance, *r* = 4.84 Å, but also a tiny nonzero value, a_{iso} = +0.01 MHz. Despite the remote position of the $^{13}C10$ of LA from the Mn^{2+} ion, a remarkable sensitivity of ENDOR spectra to distance emerges from the data.

As noted above, the high resolution of the low-field spectrum further permits the detection and characterization of a minority conformational substate that is not detected in the 2D patterns. The single-crystal-like spectrum for $^{13}C10$, Figure 6, shows such a feature on the inner shoulder of the $m_s = -5/2$ peak for the dominant (*a*) conformer. It is the $-5/2$ peak from a minority (*b*) conformer with smaller dipolar offset, $\delta\nu_{-5/2} = -5T/2$ and thus is at a greater distance from Mn: *r*(*a*) = 4.84 Å (~80% occupancy), but *r*(*b*) = 5.21 Å (~20% occupancy) (Table 2).

Table 2. Hyperfine Parameters for ^{13}C Labeled LA

			r (Å)^a	$T_{obs}{}^a$ (MHz)	ϕ, θ (deg)^b	LW^c (kHz)	δr (Å)^d	occupancy (%)^e
WT	^{13}C10	a	4.84	0.175	0, 50	60		80
		b	5.21	0.141		40		20
	^{13}C11	a	4.89	0.170	0, 40	70		50
		b	5.65	0.110^f	20, 60	60		50
DM	^{13}C10	a	4.80	0.180	0, 45	60	~0	80
		b	5.18	0.143		50	±0.06	20
	^{13}C11	b	5.80	0.102^f	20, 60	60	~0	100
I553G	^{13}C10	a	4.84	0.175	20, 45	85	±0.12	60
		b	5.23	0.139		65	±0.16	40
	^{13}C11	b	5.57	0.115^f	40, 50	65	±0.04	100
WT	^{1}H$_a{}^g$		~2.7	~4.0	0, 70	100		
	^{1}H$_b$		~2.9	~3.2	nd^h	100		

^{a}Precision of $T(r) = \pm 4$ kHz; values of r calculated assuming $\rho_{eff} = 0.994$. As described in the Supporting Information, the precision in Mn−C distances based on measurement uncertainties yields a total uncertainty of $\delta r/r \sim \pm 0.02$, corresponding to $\delta r \sim \pm 0.1$ Å for $r \sim 4.8$ Å. $a_{iso} = 0.01$ MHz, except as noted. ^{b}Error of angles = ±10° and ±5° for ϕ and θ, respectively. ^{c}Precision of ENDOR LW = ±5 kHz. ^{d}Increased distribution in Mn−C distance relative to that in WT enzyme; the changes in line width in mutant enzyme are interpreted as changes in the distribution in distances as discussed in the Supporting Information. ^{e}The occupancy of the (a) and (b) conformers is estimated by a summation of the simulation to fit the experimental spectrum at 11 000 G. Error of occupancies = ± 5%. $^f a_{iso} = 0$. ^{g}Well-defined aqua proton. ^{h}Not determined: The angles have the range of (~0, 40) to (~0, 60).
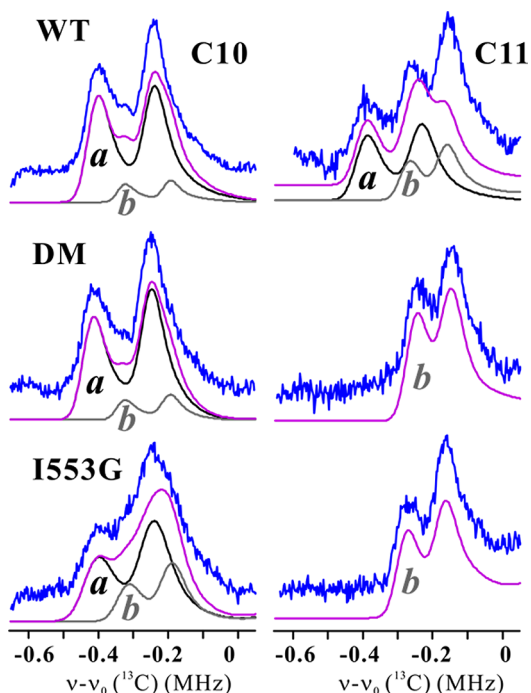
Figure 6. 35 GHz Mims ^{13}C ENDOR spectra (blue) and simulation (purple) at 11 000 G for Mn-SLO WT, DM, and I553G with ^{13}C10-LA (left) and ^{13}C11-LA (right). Conditions: same as those in Figure 5. Simulations: Experimental spectra are shown in blue, and individual simulations of conformers, (a) and (b), and the sum of these are shown in black, gray, and purple, respectively. For ^{13}C11 of DM and I553G enzymes, the spectra are simulated by a single conformer, (b). These parameters are listed in Table 2. 2D field-frequency pattern spectra and simulation are shown in Figures 5 and S6.

^{13}C11-LA. Surprisingly, in WT SLO the site of LA reactivity, C11, does not have a single well-defined majority position in the active site, even though C10 does. The low-field ^{13}C ENDOR spectrum from ^{13}C11-LA at 11 000 G has three distinct peaks, not two (Figure 6), and as shown by the simulations, this occurs because C11 adopts two equally populated locations in the active site of SLO. The (a)

conformation (~50% occupancy, Table 2) has a Mn−C11 distance almost identical to that of C10, whereas the (b) conformation places C11 nearly an angstrom farther away: $r(a)$ = 4.89 Å (~50% occupancy), but $r(b)$ = 5.65 Å (~50% occupancy) (Table 2).

^{1}H$_2$O ENDOR. To orient the C10−C11 fragment of LA relative to the Mn−OH$_2$ linkage and thereby generate the information necessary to estimate the metal-bound oxygen to carbon distance central to catalytic H atom abstraction, we carried out ^{1}H ENDOR measurements on the exchangeable protons of the bound H$_2$O, distinguishing these from the constitutive protons of coordinated histidine by subtracting spectra collected with enzyme in D$_2$O buffer from those of enzyme in H$_2$O buffer (see the Supporting Information). The ENDOR spectra that form the resulting ^{1}H 2D ENDOR pattern show two distinct ^{1}H responses, denoted ^{1}H$_a$ and ^{1}H$_b$, likely arising from the two protons of H$_2$O coordinated to Mn^{2+} or, less likely, from OH$^−$ in two conformers. Proton ^{1}H$_a$ has a distinctly better resolved ENDOR response. Its position, as determined by simulations of its 2D pattern (Figure S5), lies roughly within the x−z ZFS plane, as do those of C10 and C11 (see Table 2 for parameters and Figure 7). The peak positions and line shape for the ^{1}H$_b$ signal are not defined sufficiently enough to extract a precise location.

ENDOR of Mn-SLO Variants. *Effects of Mutations on Position of C10.* As with the WT enzyme, we collected 2 K 2D field-frequency patterns of ^{13}C ENDOR spectra taken across the EPR envelope of the Mn^{2+} ion of Mn-SLO mutants with ^{13}C10- and ^{13}C11-LA bound in the active site and used the multipass analysis protocol to generate optimized simulations of these patterns, Figure S6. The resulting ^{13}C10 and ^{13}C11 hyperfine parameters are given in Table 2.

Analogous to the WT enzyme, ^{13}C ENDOR spectra show highly resolved single-crystal-like low-field ENDOR spectra for ^{13}C10-LA bound to the DM and I553G SLO variants (Figure 6, left-hand column). Each exhibits the two single-crystal-like lines at offset $\delta\nu(m_s) = m_s \times A_\perp$ ($m_s = -5/2, -3/2$), whose frequencies can be used directly to calculate r(Mn−C10) for the main conformation. The spectrum from the DM variant is unchanged from that of the WT enzyme, thus demonstrating
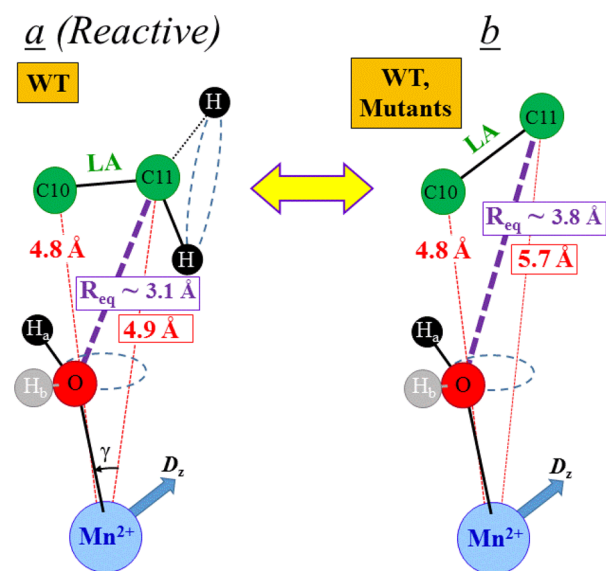
Figure 7. Model structures for active site ground state (a) and (b) conformers. The distances represented by the red dotted lines are ENDOR-derived distances; the Mn−O distance, obtained from the X-ray crystal structure, is 2.23 Å. For the (a) conformer in WT enzyme, the angle, $\gamma = 26°$, is calculated by MD simulations using ENDOR-derived distances as restraints (see Materials and Methods). The Euler angles (ϕ, θ) relative to ZFS axes for $^{13}C10$, $^{13}C11$, and $^{1}H_a$ in the WT (a) conformer are (0°, 50°), (0°, 40°), and (0°, 70°), respectively; the shared values of $\phi \sim 0$ imply that all three lie, within error, in the $x−z$ plane of the ZFS tensor. The position of $^{1}H_b$ is not well established, and it is arbitrarily pictured (in gray), for completeness, since the active site 2+ metal ion is anticipated to bind a water molecule. The purple dashed line represents the ground state equilibrium DAD distance (R_{eq}) calculated trigonometrically. The DAD (R_{eq}) for the WT (b) conformer (purple dashed line) is estimated by also assuming $\gamma = 26°$. MD simulations on the I553G and DM structures (see Materials and Methods) produce comparable γ values (31−33°) to WT. Using $\gamma = 26°$ (from WT) yields DADs of 3.7 and 3.9 Å, respectively, for I553G and DM SLO (b) conformers. The uncertainty of the C11−O distances is estimated as ±0.2 Å (see the text and Supporting Information). Dashed circles suggest the nuclei (oxygen of water and C11 hydrogens in (a) conformer) lie out of the $x−z$ plane of the ZFS axes.

that replacement of this pair of residues, which includes the L754A replacement adjacent to the metal-ion site, nonetheless does not alter either the occupancies of the majority (a) and minority (b) positions of C10 or their Mn−C10 distances (Table 2).

In contrast, the low-field $^{13}C10$ ENDOR spectrum is obviously altered by the I553 variation. The peak frequencies for the reactive (a) conformer are also essentially unchanged relative to WT, which shows that the mutation does not alter the Mn−C10 distance for this conformer (Table 2). However, the spectra clearly show the presence of features with lower offset, associated with an enhanced population of the (b) conformer at a substantially longer Mn−C10 distance (Table 2). In addition, the features of both conformers for I553G are strongly broadened, which implies that each "conformer" in fact corresponds to a distribution of Mn−C10 distances whose breadth is increased by the mutation (see the Supporting Information).

Loss of the (a) Conformer for C11 in I553G and DM-SLO. The low-field $^{13}C11$ spectra of I553G/LA and DM/LA show that both variations depopulate the near-lying (a) conforma-

tion, leaving the (b) conformation, with its larger Mn−C11 distance unchanged (Figure 6, right-hand column). An unchanged line width for (b) further indicates that in both variants the distribution of distances for this conformation remains the same. This result implies that restraints in the WT enzyme ground conformational state force the LA in approximately half of the ES complexes to adopt the (a) conformation with its shorter Mn−C11 distance, $r = 4.89$ Å, whereas LA in the other half of the ES complexes adopts the (b) conformation with its longer distance, $r = 5.65$ Å. The packing defects created by either the I553G or DM mutations relax those restraints and allow the enzymatic target C11 carbon of LA to "spring back" from what is clearly the reactive, (a), conformation, leading to essentially complete occupancy of the more remote, inactive (b) conformation. Thus, the positioning of C11 changes sharply in both mutants, but that of C10 does not.

MD Simulations on Mn-SLO/LA Model. To convert the metal-to-carbon distances obtained from ENDOR measurements to ground state carbon (proton donor) to oxygen (proton acceptor) distances, it was necessary to estimate the internal angle among C11, Mn, and the oxygen of the water bound to Mn (see Figure 7). This was accomplished via in silico modeling of the SLO/LA complex using the WT Mn-SLO crystal structure to obtain the starting coordinates and imposing ENDOR restraints on the C11−Mn and C10−Mn distances during MD simulations. In these calculations, two orientations of the LA within the binding pocket were considered: with the carboxylate group buried ("carboxylate in") or pointing toward the surface ("carboxylate out").[28] A variety of structural studies with substrate analogues and also kinetic studies have suggested the possibility of both orientations.[27,28,60−63] Because of the resulting uncertainty regarding the correct binding mode in SLO, the MD simulations were thus conducted for both possible orientations of LA.

For the reported MD simulations, the protein was treated using the AMBER12 force field with additions described in the Supporting Information, and the system was solvated with explicit TIP3P water molecules. The C11−Mn and C10−Mn WT distances were restrained to the "close" values determined from the ENDOR experiments, at 4.9 and 4.8 Å for C11−Mn and C10−Mn, respectively, by applying harmonic restraints. After a comprehensive equilibration procedure, two independent 50 ns trajectories were propagated for each system, and representative configurations for each system are shown in Figure S7. For the "carboxylate-in" model, the DAD (C11−O distance) in the ground state was calculated from the ENDOR-derived Mn−^{13}C distance and the MD-derived O−Mn−^{13}C angle: $R_{eq} \approx 3.1$ Å, with an uncertainty of ∼0.2 Å arising from a combination of the uncertainties in the angle (±4°) and the ENDOR measurements (±0.1 Å). The average C11−O distance obtained from the equilibrium MD simulations with ENDOR-derived restraints was also 3.1 Å (Table S4). This DAD of 3.1 Å corresponds well to a sum of van der Waals radii. However, the MD simulations on the "carboxylate-out" orientation resulted in a much longer equilibrium C11−O distance of 4.2 Å for WT SLO. This latter model also places C13, the selective site for molecular oxygen insertion upon radical formation, away from the putative O$_2$ channel.[64] Therefore, our MD simulations provide preference for a "carboxylate-in" binding orientation for LA in SLO. The

1991

remainder of this discussion will thus pertain to the "carboxylate-in" binding orientation.

MD simulations were also performed for the Mn^{2+}-containing I553G and DM-SLO systems in a similar manner to WT (see the Supporting Information). The C11–Mn and C10–Mn distances were restrained to the values determined from the ENDOR experiments: the C11–Mn distances were ca. 5.6 and 5.8 Å for the I553G and DM species, respectively, and the C10–Mn distance was 4.8 Å for both species. These distances correspond to the (b) conformation, in contrast to the distances corresponding to the (a) conformation used for WT. The MD simulations indicate that the C11–Mn–O angles are within error for the WT and mutant proteins, Table S4, whereas the C11–O distances for the two mutant species are of course longer, Table S4, mainly due to the use of restraints associated with the more highly populated (b) conformation.

■ DISCUSSION

This work marks the inaugural report on the active site geometries for the ES complex of SLO. A picture of the active site of SLO/LA is generated by this study (Figure 7) through a combination of (i) 35 GHz pulsed ENDOR measurements of the length and orientation of the vectors from the active site Mn^{2+} to C11 and C10 of LA and the ^1H of bound H_2O (Table 2); (ii) the X-ray structure of Mn-SLO, which makes it clear that Mn substitution provides a faithful structural analogue to the native SLO and gives the Mn–O distance; (iii) a value for the angle, γ, subtended by the Mn–O vector and the Mn–C11 vector as inferred from the "carboxylate-in" MD simulation of Mn-SLO/LA; and (iv) the assumption of standard bond lengths and angles for the atoms of LA and the bound water. Creation of this picture was greatly simplified by the ENDOR result that C11, C10, and one of the H atoms of H_2O all lie in the same plane (Figure 7).

The ENDOR measurements determine hyperfine coupling tensors of the nearby noncoordinated nuclei through the analysis of the 2D field-frequency pattern of orientation-selective ENDOR spectra collected across the EPR envelope of the Mn^{2+} ion of Mn-SLO (Figures 5 and 6). The dipolar interaction component of the coupling to ^{13}C nuclei of bound LA substrate and ^1H of bound water/hydroxide, **T** (eq 2), yields both the length and orientation of the Mn-nuclear vector relative to the ZFS axes. Analysis of analogous 2D patterns for paramagnetic centers whose anisotropic g tensor introduces orientation selection into the individual ENDOR spectra has been increasingly utilized since the protocol was first introduced.[57] However, although it was noted at that time that "the same approach could be used in cases where fine-structure [ZFS] anisotropy dominates",[57] to our knowledge this is the first instance where this possibility has been realized. The overlap of EPR signals from the multiple m_s manifolds of the $S = 5/2$ Mn^{2+} adds a substantial degree of difficulty to this ZFS approach. However, by taking into account strong enhancement of sublevel and orientation selectivity in the EPR signal achieved by the thermal depopulation of higher-lying m_s levels at 2 K, we have been able to use the resulting enhanced orientation selectivity in the ENDOR responses to determine the hyperfine coupling matrices for the Mn-SLO substrate nuclei and for bound water as well. The development of this protocol has allowed us to use the through-space dipolar coupling to the substrate to obtain precise metrical data for the distance of the C11 target and adjacent C10 of LA from the metal ion, as well as their orientation relative to the H_2O ligand.

Embedding these results into the X-ray and "carboxylate-in" MD structures then yields the pictures of substrate binding presented in Figure 7 that incorporates the metrical values summarized in Table 2.

Three key features emerge from the current study, as visualized in Figure 7. First, the equilibrium DAD (R_{eq}) in the dominant ground state conformation of the WT SLO enzyme–substrate complex indicates a van der Waals contact between the target C11 of the substrate and the oxygen of the ligated water molecule, $R_{eq} \sim 3.1$ Å; a minority ground state conformation, (b), has an even larger distance, $R_{eq} \sim 3.8$ Å. We note that these are the minimum distances that arise from the planar arrangement of atoms illustrated in Figure 7. Some deviation from planarity is expected as the active site geometry is optimized for orbital overlap between the transferred hydrogen and the lone pair of the acceptor oxygen atom, and this would increase the distances. This finding demonstrates the need for conformational sampling to achieve configurations with the decreased proton donor–acceptor (C11–O) distance (ca. 2.7 Å in the WT enzyme) required for effective tunneling in nonadiabatic hydrogen tunneling models. As discussed in depth in a number of reviews (e.g., refs 11, 18, and 65), the hydrogen vibrational wave function overlap between reactant and product states depends on the proton DAD, which fluctuates due to equilibrium thermal motions, thereby sampling shorter distances with higher tunneling probabilities.

Second, the observed ground state equilibrium C11–O distances in strategically placed mutations are elongated with respect to WT (enhanced occupancy of the (b) conformation, which has $R_{eq} \sim 3.8$ Å). Third, the increase in the ground state distance dispersion for $^{13}C10$ LA in the I553G mutant, relative to WT or DM, is in the direction expected from the previous observation of a weaker force constant for donor–acceptor sampling and, hence, enhanced sampling that helps to recapture some of the DAD characteristic of WT (cf. δr values in Table 2). These aggregate findings provide strong support of the theoretical framework that has been previously advanced for C–H activation in lipoxygenase.[19−22,66]

Absence of Compaction in the WT-SLO Ground State ES Complex. The ground state active site structure trapped by freezing the LA complex of WT enzyme exhibits substrate positioned in two (major) conformations. The most significant finding from the WT enzyme is that the distance from the reactive C11 of LA to the oxygen of the metal-bound water is $R_{eq} \sim 3.1$ Å in the closer (a) conformation, meaning that the transferred hydrogen would still need to move ca. 1.0 Å and even longer to the extent that reaction occurs from a position outside of the Mn–C10–C11 plane. We are, thus, able to rule out any unusual "compaction" within the dominant ground state enzyme–substrate complexes of SLO, providing experimental confirmation that the short tunneling distances predicted for catalytic hydrogen atom tunneling (ca. 0.6 Å) must arise from the sampling of the protein–ligand conformational landscape accessible within the ES complex. In the (b) conformation of LA, although C10 of LA remains at essentially the same position as in the (a) conformation, the target C11 of substrate has "sprung away" from the reactive oxygen by an additional ~0.7 Å. In order for SLO to react from this extended (b) conformation, a much more significant protein structural rearrangement will be required that may be better described as a protein conformational change that first converts (b) into the (a) conformation prior to the conformational "fine-tuning".

In considering catalytic function, it is important to note that over the course of the two 50 ns MD trajectories conducted on the WT system (Figure S8) 4 out of 2000 frames (0.2%) displayed DADs that are ≤2.9 Å, with the shortest at 2.88 Å. Although we would not expect the shorter distances to be sampled more than a few times (at most) in the complete 100 ns simulations, the observation of C11−O distances at ≤2.9 Å establishes some precedent for the role of stochastic protein−ligand thermal motions in forming compacted DADs during the reaction. Given the wide range of time scales for protein motions that are expected to occur, longer MD simulations on SLO will be of considerable interest.

We note that while the present measurements are focused on the DAD, the efficiency of hydrogen tunneling will also be dependent on protein motions that give rise to electrostatic tuning, normally represented by the reorganization energy and reaction free energy as originally derived in the context of the Marcus theory of electron tunneling.[67]

Relevance to Other C−H Activating Enzymes. While "ES" structures of human lipoxygenases have been reported,[68−70] perhaps the only true ES model of lipoxygenases thus far is the coral 8R-lipoxygenase with bound arachidonic acid.[63] This lipoxygenase and SLO share only 28% sequence identity, react with different substrates, and have distinct kinetic behaviors. However, the iron in 8R-lipoxygenase maintains proper octahedral geometry with the expected conserved iron ligands, and the atomic coordinates of the metal and the first ligation sphere are nearly superimposable with native SLO (RMSD = 0.24 Å). From this X-ray derived model, the ground state DAD between reactive carbon (C13) of arachidonic acid and oxygen from the water bound to Fe is 3.4 Å (beyond van der Waals contact) and is qualitatively comparable with our current findings.[63]

The observation here of van der Waals contacts within the SLO ES complex provides a direct correspondence with the X-ray derived ES structures of other types of C−H activating enzymes, for example, dihydrofolate reductase (DHFR), which has served as one of the model enzymes for quantum mechanical hydride (charged atom) transfer studies. Although the electrostatics of the active site are considerably different than SLO, native DHFR displays temperature-independent kinetic isotope effects,[71] suggesting the importance of isotope-independent conformational sampling modes to achieve tunneling-effective DADs that are significantly shortened from the ground state with van der Waals contacts.[17,72] Thus, a unified picture has emerged for C−H activating enzymes, in which stochastic sampling of a range of protein−ligand conformational substates is a necessary prerequisite for effective hydrogen tunneling.[10,11,73,74]

Effects of Mutants on the Ground State DAD and Relevance to Catalysis. Having characterized the active site ES structure in WT SLO, the DADs of two previously studied mutants with sharply altered catalytic properties were likewise examined. Position 553 is expected to interact with substrate, but it is remote from the site of hydrogen abstraction (the nearest side chain atoms are ≥10 Å from the Fe center in SLO). Extensive kinetic and theoretical investigations[21,22,25] have led to the conclusion that mutations at this position both increase the equilibrium ground state DAD, through an enlargement of the active site cavity, and also permit more facile DAD sampling that enables some recovery of WT behavior. These effects are manifested primarily in the temperature dependence of the kinetic isotope effect (ΔE_a), which increases from an apparent

difference in activation energy of 0.9 kcal/mol for WT to 5.3 kcal/mol for the most extreme variant, I553G.[25] The second variant studied, the double mutant (DM-SLO), constructed by changing two conserved leucine residues proximal to the site of hydrogen abstraction into alanines (L546A/L754A; Figure 1A), exhibits an impaired k_{cat} that is 10^4-fold lower than WT and an unprecedented kinetic isotope effect (>500) at room temperature.[42] Analysis of DM-SLO kinetics[22,42] compared to WT kinetics indicates an increase in the R_{eq}, which is consistent with the enlarged active site cavity, and similar or less facile DAD sampling, thereby precluding recovery of WT-like behavior as seen for I553X.

For both of these variants, the ENDOR measurements show that the mutation depopulates the LA (a) conformation with closer approach of C11 to Mn seen in WT enzyme, leaving only the (b) conformation with the longer distance. We interpret these changes in LA conformation within the I553G and DM of Mn-SLO as reflective of a balance in the native protein between forces exerted by nearby amino acid residues that stabilize the close (a) conformation and a range of additional substrate/protein interactions that can torsion the LA chain away from the metal center when key restraints are removed. For example, when the forces exerted by I553 are "relaxed" in the I553G variant, which opens the pocket in the vicinity of bound substrate, the reactive carbon "springs back" and the C11−C10 fragment adopts only the (b) conformation, with negligible occupancy of the reactive (a) conformation. In contrast, the C10−Mn distances are not significantly perturbed upon mutation, supporting a remarkable specificity of structural forces in WT that control the geometry of the reactive carbon (C11) of substrate within the active site cavity.

In these SLO mutant enzymes, the loss of the (a) conformer for the C11−Mn interaction leads to C11−O distances that are ~0.7 Å longer than WT (3.7 and 3.9 Å) for I553G and DM variants, respectively. These longer DADs are not conducive to facile hydrogen transfer and, as already noted in the context of WT-SLO, require a transformation from the (b) conformer to the reactive (a) conformer to facilitate sampling of yet shorter distances that can support hydrogen transfer. Vibronically nonadiabatic theoretical models of SLO lead to DAD dominant tunneling distances in the range of ca. 2.7 Å in the native enzyme to ca. 2.9 Å in selected mutants, requiring a balance between more remote conformational sampling processes and local DAD sampling, with the latter becoming especially critical for obtaining distances conducive to facile hydrogen tunneling in the majority of mutants.[22,66]

The fundamental kinetic differences between the roles of the DAD in I553G vs DM-SLO are fully supported by the ENDOR experiments. In the case of the I553G variant, a broadening of the ENDOR lines implies a general loosening of bound substrate that produces an increased distribution in the ^{13}C10−metal ion distances and hence the hyperfine couplings, eq S11. These changes are consistent with published kinetic data that have implicated a significant increase in active site flexibility that imparts enhanced sampling of the DAD in I553G.[21,22,25] The properties of the ground state ES complex as inferred from the nonadiabatic kinetic analysis of DM are quite distinct from I553G, with a similar expectation of an elongated DAD but with a reduced capability for recovery of the shorter DAD characteristic of WT SLO.[22,42] It is therefore gratifying to see that the ENDOR spectra for both C10 and C11 of the substrate with DM-SLO are consistent with a less flexible positioning of the substrate relative to the catalytic metal center that

approximates WT. It follows that the magnitude of the distance dispersion of the ENDOR spectra may serve as a potentially new, sensitive probe for changes in substrate dynamics or flexibility within an active site cavity.

■ CONCLUSIONS

The three-dimensional SLO active site ground state has been shown to contain a reactive conformer with a hydrogen DAD of ~3.1 Å, approximately van der Waals contact, as well as an inactive conformer with an even longer DAD, establishing that stochastic conformational sampling is required to achieve reactive tunneling geometries. Tunneling-impaired SLO variants show increased DADs and variations in substrate positioning and rigidity, confirming previous kinetic and theoretical predictions of such behavior. The present investigation highlights (i) the high degree of predictive power that is emerging from developed nonadiabatic quantum treatments of proton-coupled electron transfer (PCET) in SLO (and other systems) and (ii) the sensitivity of ENDOR probes to test, detect, and corroborate kinetically predicted trends in the physical parameters that describe active site reactivity and to reveal unexpected features of active site architecture.

■ MATERIALS AND METHODS

Materials. The synthesis for specifically labeled $^{13}C10$ LA and $^{13}C11$ LA has been previously reported.[76] The positions of the isotopically labeled substrates are shown in Figure S9. Manganese(II) chloride was obtained from Strem Chemicals (99.999% Mn). Unless noted, all other reagents were obtained from Sigma-Aldrich, Fisher Scientific, or VWR.

Protein Expression and Purification. Wild-type and mutant SLOs were expressed in *E. coli* BL21(DE3) Codon Plus RIL cells. Overnight cultures (120 mL), generated from fresh transformations and grown in LB/Amp medium, were centrifuged to remove enriched medium. Cells were washed and resuspended in (6) to (12) 1 L M9-based minimal media, devoid of iron, but containing 0.4% (w/v) glucose and supplemented with 1 mM magnesium sulfate, 0.1 mM calcium chloride, 100 μg/mL thiamine, 150 μM manganese(II) sulfate, and 0.2% (w/v) casamino acids. The cultures were grown to OD_{600} = 0.6−1.0, at which point the temperature was rapidly decreased to 15 °C and maintained for 96 h. The cultures were harvested; SLO was purified as described previously.[42] Typical yields were 0.5−3 mg of SLO per liter. All proteins were 90% pure, as assessed by SDS-PAGE analysis.

Manganese Incorporation Quantitation. Metal content was determined using inductively coupled plasma−atomic emission spectroscopy (ICP-AES), which was performed at the Inductively Coupled Plasma Spectroscopy Facility in the College of Natural Resources, UC Berkeley. Manganese and iron concentrations were determined from standard curves using 10, 50, 100, 500, and 1000 ppb Mn/Fe dilutions of commercially available 1000 ppm metal reference standards (Fisher Scientific). Protein concentrations were determined using the molar extinction coefficient ε_{280} = 132 mM^{-1} cm^{-1}.[77] The manganese contents, averages of three replicates each, were determined as 0.9 ± 0.1, 0.6 ± 0.05, and 0.6 ± 0.1 Mn^{2+} atoms per protein for WT, DM, and I553G manganese-substituted samples, respectively. All samples contained ca. 0.03 ± 0.03 iron per Mn-SLO. For comparison, the iron content for WT Fe-SLO was measured with both ICP-AES and the ferrozine assay.[78] Both methods gave similar results, with 0.9 ± 0.1 Fe atoms per WT Fe-SLO.

UV Kinetics. To test the level of activity in the WT Mn-substituted SLO, steady-state kinetic experiments were conducted spectrophotometrically on a Cary 50 UV/vis spectrophotometer as described previously.[19] Product, hydroxyoctadecadienoic acid (HPOD), formation was quantified from the absorbance at 234 nm with a molar extinction coefficient ($\varepsilon_{234\ nm}$ = 23.6 mM^{-1} cm^{-1}). Unimolecular rate constant (k_{cat}) for Mn-SLO at 30 °C was determined to be ca. 7 ± 2

s^{-1}, which is 2−3% of WT Fe-SLO. Because this value coincides with the level of contaminating iron (see above for ICP-OES results) and is much lower than the rate of linoleic acid (per)oxidation by the native MnLOX (k_{cat} ~ 20−30 s^{-1}; see Table S1), we conclude that Mn-SLO is inactive.

Cryogenic X-ray Crystallography. All additional protein purification and crystallization steps were performed as previously described,[25] with modifications.[42,79] After several rounds of seeding, the crystals were transferred to 20% PEG-3350, 0.2 M sodium acetate, pH 5.5, and 20% ethylene glycol and then flash frozen in liquid N$_2$. Diffraction data were collected at 100 K at beamline 8.3.1 of the Advanced Light Source at Lawrence Berkeley National Laboratory. All data were processed at the College of Chemistry Molecular Graphics Facility (UC Berkeley) using the CCP4 suite,[80] with integration performed in IMOSFLM[81] and scaling and merging in POINTLESS, AIMLESS,[82,83] and CTRUNCATE.[84,85] An initial solution was found by molecular replacement using Phaser[86] with PDB 3PZW as the search model. Manual refinement was performed in Coot,[87,88] and automated refinement, using the PHENIX suite.[89]

ENDOR Sample Preparation. ENDOR samples contained 500 μM Mn-SLO and 1 equiv of respective LA in 0.1 M sodium borate, pH 9.0, with 15% (v/v) ethylene glycol as a glassing agent. To prepare each sample, a known amount of LA, determined enzymatically, was transferred to a glass vial then to an anaerobic glovebox. LA was dissolved in deoxygenated 0.1 M sodium borate, pH 9.0, containing 50% (v/v) ethylene glycol. The LA/ethylene glycol solution was mixed with deoxygenated enzyme to a total volume of 65 μL and 15% (v/v) ethylene glycol and transferred into a suitable ENDOR tube. The tube was sealed with vacuum grease, removed from the glovebox, and frozen in liquid nitrogen within 30 s of its removal. The samples were stored at liquid nitrogen temperature until data acquisition. A control experiment, in which an ENDOR sample was prepared as described above but within a UV/vis cuvette, was sealed and removed from the anaerobic chamber and scanned spectrophotometrically for the presence of product (234 nm). No product formation was detected over the course of 45 min at room temperature. Product began to form once the cuvette was opened to atmospheric oxygen. This control demonstrates that there is no detectable product formation during the time course of the ENDOR sample preparation. It is important to note that, under the buffer conditions listed above, the critical micelle concentration (CMC) of LA is >0.6 mM, as determined by steady-state fluorescence techniques with 1,6-diphenyl-1,3,5-hexatriene as a sensitive fluorescent reporter of micelle formation.[90] Furthermore, control kinetic experiments were conducted with the ENDOR buffer conditions (0.1 M sodium borate, 15% ethylene glycol, pH 9.0) and showed comparable kinetics to standard kinetic reaction buffer conditions, which lack 15% ethylene glycol.

For the D$_2$O-exchanged SLO experiment, the samples were prepared as described above for the specific label, except with a D$_2$O-exchanged protein. The WT Mn-SLO was exchanged into 0.1 M borate pD 9.0 (using corrected pH reading[91]) D$_2$O (Cambridge Isotopes, 99% D) buffer via four cycles of dilution and concentration via 15 mL Amicon 30K MWCO centrifuge concentrator. Prior to mixing anaerobically, natural abundance LA was prepared in deoxygenated 0.1 M borate pD 9.0 containing 50% (v/v) ethylene glycol-(OD)$_2$ (Isotech; 98% D).

EPR/ENDOR Measurements. Q-band CW EPR spectra were collected on a spectrometer described previously.[92] Q-band echo-detected EPR spectra (two-pulse echo sequence, $\pi/2-\tau-\pi-\tau$-echo) and pulsed ENDOR[93] spectra were collected on a spectrometer that has similarly been described.[94,95] All measurements were done with helium immersion dewars, at 2 K. The Davies sequence (three-pulse echo sequence, $\pi/2-\tau-\pi-T-\pi/2-\tau$-echo, with rf pulse ($T_{rf}$) inserted in the interval, T, between second and third pulses[93]) was used for ^{1}H and ^{14}N ENDOR of H$_2$O and histidine coordinated to Mn^{2+}.[39,41] The Mims pulsed ENDOR sequence (three-pulse echo sequence, $\pi/2-\tau-\pi/2-T-\pi/2-\tau$-echo, with rf pulse ($T_{rf}$) inserted in the interval, T, between second and third pulses[93]) was used for ^{13}C ENDOR of labeled LA substrate.

EPR Simulations. The zero-field splittings (ZFS) of the Mn^{2+}-SLO variants were obtained by best fitting the "shoulders" and "wings" of their 2 K absorption-display EPR spectra with the EasySpin 5.0 program in Matlab, as modified by incorporation of a Gaussian distribution in the ZFS parameters, [D, λ] (Supporting Information). This procedure nicely reproduces the main features in a spectrum, but fine details of the intensities are not perfectly matched. In part this is because the distribution is not a simple Gaussian, but in larger part this is because "the spectrum" of Mn^{2+} ($S = 5/2$) at 2 K is not itself well-defined. The detailed shapes of both CW and pulse EPR spectra depend sensitively on relaxation processes that are neither understood in detail nor incorporated in the computer simulations.

ENDOR Simulations. ENDOR spectra were fit with EasySpin 5.0, with the use of the distributed ZFS parameters determined in the EPR simulations (Supporting Information), and the incorporation of "blind spots" in Mims ENDOR spectra through a modification for $S > 1/2$ systems of the procedures described previously.[96] Optimization of spin-Hamiltonian parameters gives essentially perfect agreement with frequencies of features in the ENDOR spectra but, at best, adequate agreement with intensities. We attribute this to difficulties similar to those that hamper simulation of EPR spectra. In determining relative occupancies of the different conformers, we use only the intensities of the $m_s = -5/2$ peaks obtained at the low-field single-crystal-like edge of the EPR spectrum (11 000 G), Figure 6; for this comparison, effects of the difficulties cancel.

As described in Results, and with further details given in the Supporting Information, the ZFS of the $S = 5/2$ Mn^{2+} ion introduces strong sublevel and orientation selectivity in the EPR signal, enhanced by the thermal depopulation of higher-lying m_s levels at 2 K, and this translates to corresponding selectivity in the ENDOR responses, allowing analysis of the dipole-dominated hyperfine tensor through analysis of 2D field-frequency plots, in analogy to the approach used in the simpler case of $S = 1/2$.[59]

Computational Details. The MD simulations were performed using NAMD-2.9.[97] For the WT enzyme, the initial structure was obtained from the Mn-SLO crystal structure with PDB code 4WFO. For the I553G and DM mutant Mn-SLO species, the corresponding mutant Fe-SLO crystal structures were used as starting structures (PDB code 3BNC for the I553G mutant[25] and 4WHA for DM[42]), replacing the Fe with Mn and optimizing the geometry of the replaced Mn and surrounding six ligands with the remainder of the enzyme structure fixed. It is important to note here that these geometry-optimized Mn^{2+} ion containing structures of the I553G and DM variants reproduce the short Asn694—metal distance as seen in the X-ray structure of WT Mn-SLO (for more information, see the analysis of the Mn-SLO structure in the Results section). The missing residues in the 4WFO crystal structure were added with the Profix module in the Jackal package.[98,99] The protonation states of each residue were determined and the hydrogen atoms were added using the H++ utility[100,101] with pH = 9.0. The initial position of the LA substrate was determined by docking the substrate to the active site of the Mn-SLO using the Glide module in the Schrödinger package.[102]

The AMBER12 force field[103–106] was used to describe the majority of the system, with additional parameters determined as follows. The partial charges of the atoms in the LA substrate were obtained from a previous study.[107] The parameters for the equilibrium Mn—ligand bond lengths were obtained from a QM/MM geometry optimization, in which the Mn and the six ligands (i.e., residues 499, 504, 690, 694, and 839 and the bound water) were in the QM region and all other atoms were in the MM region. The QM region was treated with density functional theory using the B3LYP functional in conjunction with the 6-31G** basis set for all atoms with the exception that the LANL2DZ[108] basis set was used for the Mn atom. The force constant parameters for the Mn—ligand bonds were obtained from a previous experimental study for a Mn model compound.[109] In contrast to the Mn—ligand bond parameters, which were specific to the Mn system, the Mn—ligand angle (X—Mn—Y, where X and Y are the ligand atoms bound to Mn, and Mn—O—H for the water ligand) parameters were approximated to be independent of the metal center and were chosen to be identical to those used in previous studies of the Fe-based

system.[20,107] The bond and angle parameters associated with the Mn—ligand interactions are provided in Table S3. The explicit water was described with the TIP3P water model.[110]

The computational details of the equilibration procedure and the subsequent MD trajectories are as follows. First, only the positions of the hydrogen atoms were optimized while the other atoms in the system were fixed. Next, the Mn-SLO system was solvated in a TIP3P[110] water box with dimensions 134 × 90 × 80 Å^3, and the system was neutralized by adding sodium ions. In the first stage of equilibration, only the water and sodium ions were equilibrated at 300 K in the NVT ensemble for 100 ps, while the Mn-SLO/LA portion of the system was fixed. At this point in the procedure, the C11—Mn and C10—Mn distances were restrained to the values determined from the ENDOR experiments by applying harmonic potentials to prevent ligand dissociation. The equilibrium C11—Mn distance was set to be 4.9, 5.6, and 5.8 Å for the WT, I553G, and DM Mn-SLO species, respectively, and the C10—Mn distance was set to be 4.8 Å for all three species. The force constant used for these harmonic restraints was 200 kcal/mol Å^{-2}. Prior to performing MD, first only the geometry of the LA substrate was optimized while the Mn-SLO and solvent were fixed, and subsequently the whole system was optimized. In the next stage of equilibration, the temperature was raised incrementally from 50 to 100, 200, and 303 K with 100 ps of MD at each temperature in the NVT ensemble. Subsequently, 1 ns of MD in the NPT ensemble at 300 K was performed. Then, another 50 ns of MD in the NVT ensemble at 300 K was conducted. After this equilibration, the production MD trajectory was propagated in the NVT ensemble at 300 K for 50 ns. One-thousand frames separated by 50 ps within the production trajectory were collected for calculating the average C11—O distance and C11—Mn—O angle. Two independent MD trajectories were propagated for each system.

■ ASSOCIATED CONTENT

Ⓢ Supporting Information

The Supporting Information is available free of charge on the ACS Publications website at DOI: 10.1021/jacs.6b11856.

> Extended description of the orientation-selection analysis of the $S = 5/2$ Mn^{2+} EPR, error analysis of Mn—C distances, and further analysis of the orientation of bound water; idealized and simulated Mn^{2+} EPR spectra of WT, I553G, and DM SLO; ^{1}H and ^{14}N Davies ENDOR spectra; 2D ^{13}C Mims ENDOR spectra of DM and I553G with ^{13}C10 and ^{13}C11; ^{1}H Davies ENDOR for WT Mn-SLO in ^{1}H$_2$O vs ^{2}H$_2$O and difference spectra; final frames of MD simulations; MD distances and angles; and extended data tables (PDF)

■ AUTHOR INFORMATION

Corresponding Authors
*klinman@berkeley.edu (J.P.K)
*bmh@northwestern.edu (B.M.H.)

ORCID Ⓘ
Masaki Horitani: 0000-0002-8881-0600
Sharon Hammes-Schiffer: 0000-0002-3782-6995
Brian M. Hoffman: 0000-0002-3100-0746

Present Addresses
∞M.H.: Department of Applied Biochemistry and Food Science, Saga University, Saga, 840-8502 Japan
#C.A.M.C.: Riffyn, Oakland, California 94612, United States
¶G.E.C.: Max Planck Institute for Chemical Energy Conversion, Stiftstr. 34—36, D-45470 Mülheim an der Ruhr, Germany

Author Contributions
⊥M.H. and A.R.O. contributed equally.

Notes

The authors declare no competing financial interest.

■ REFERENCES

(1) Edwards, D. R.; Lohman, D. C.; Wolfenden, R. *J. Am. Chem. Soc.* **2012**, *134*, 525−531.

(2) Jiang, L.; Althoff, E. A.; Clemente, F. R.; Doyle, L.; Röthlisberger, D.; Zanghellini, A.; Gallaher, J. L.; Betker, J. L.; Tanaka, F.; Barbas, C. F., III; Hilvert, D.; Houk, K. N.; Stoddard, B. L.; Baker, D. *Science* **2008**, *319*, 1387−1391.

(3) Röthlisberger, D.; Khersonsky, O.; Wollacott, A. M.; Jiang, L.; DeChancie, J.; Betker, J. L.; Gallaher, J. L.; Althoff, E. A.; Zanghellini, A.; Dym, O.; Albeck, S.; Houk, K. N.; Tawfik, D. S.; Baker, D. *Nature* **2008**, *453*, 190−195.

(4) Renata, H.; Wang, Z. J.; Arnold, F. H. *Angew. Chem., Int. Ed.* **2015**, *54*, 3351−3367.

(5) Warshel, A.; Sharma, P. K.; Kato, M.; Xiang, Y.; Liu, H.; Olsson, M. H. M. *Chem. Rev.* **2006**, *106*, 3210−3235.

(6) Fried, S. D.; Bagchi, S.; Boxer, S. G. *Science* **2014**, *346*, 1510−1514.

(7) Hilvert, D. *Annu. Rev. Biochem.* **2013**, *82*, 447−470.

(8) Kiss, G.; Çelebi-Ölçüm, N.; Moretti, R.; Baker, D.; Houk, K. N. *Angew. Chem., Int. Ed.* **2013**, *52*, 5700−5725.

(9) Frushicheva, M. P.; Mills, M. J. L.; Schopf, P.; Singh, M. K.; Prasad, R. B.; Warshel, A. *Curr. Opin. Chem. Biol.* **2014**, *21*, 56−62.

(10) Klinman, J. K. *Chem. Phys. Lett.* **2009**, *471*, 179−193.

(11) Klinman, J. K.; Kohen, A. *Annu. Rev. Biochem.* **2013**, *82*, 471−496.

(12) Allemann, R. K.; Scrutton, N. S. *Quantum Tunneling in Enzyme-Catalyzed Reactions*; Royal Society of Chemistry: London, 2009.

(13) Hay, S.; Scrutton, N. S. *Nat. Chem.* **2012**, *4*, 161−168.

(14) Zhang, J.; Klinman, J. K. *J. Am. Chem. Soc.* **2011**, *133*, 17134−17137.

(15) Zhang, J.; Kulik, H. J.; Martinez, T. J.; Klinman, J. K. *Proc. Natl. Acad. Sci. U. S. A.* **2015**, *112*, 7954−7959.

(16) Knapp, M. J.; Klinman, J. K. *Eur. J. Biochem.* **2002**, *269*, 3113−3121.

(17) Hammes-Schiffer, S. *Acc. Chem. Res.* **2006**, *39*, 93−100.

(18) Klinman, J. K. *Biochemistry* **2013**, *52*, 2068−2077.

(19) Knapp, M. J.; Rickert, K. W.; Klinman, J. K. *J. Am. Chem. Soc.* **2002**, *124*, 3865−3874.

(20) Hatcher, E.; Soudackov, A. V.; Hammes-Schiffer, S. *J. Am. Chem. Soc.* **2007**, *129*, 187−196.

(21) Edwards, S. J.; Soudackov, A. V.; Hammes-Schiffer, S. *J. Phys. Chem. B* **2010**, *114*, 6653−6660.

(22) Soudackov, A. V.; Hammes-Schiffer, S. *Faraday Discuss.* **2016**, *195*, 171−189.

(23) Minor, W.; Steczko, J.; Stec, B.; Otwinowski, Z.; Bolin, J. T.; Walter, R.; Axelrod, B. *Biochemistry* **1996**, *35*, 10687−10701.

(24) Tomchick, D. R.; Phan, P.; Cymborowski, M.; Minor, W.; Holman, T. R. *Biochemistry* **2001**, *40*, 7509−7517.

(25) Meyer, M. P.; Tomchick, D. R.; Klinman, J. K. *Proc. Natl. Acad. Sci. U. S. A.* **2008**, *105*, 1146−1151.

(26) Youn, B.; Sellhorn, G. E.; Mirchel, R. J.; Gaffney, B. J.; Grimes, H. D.; Kang, C. *Proteins: Struct., Funct., Genet.* **2006**, *65*, 1008−1020.

(27) Skrzypczak-Jankun, E.; Bross, R. A.; Carroll, R. T.; Dunham, W. R.; Funk, M. O., Jr *J. Am. Chem. Soc.* **2001**, *123*, 10814−10820.

(28) Coffa, G.; Imber, A. N.; Maguire, B. C.; Laxmikanthan, G.; Schneider, C.; Gaffney, B. J.; Brash, A. R. *J. Biol. Chem.* **2005**, *280*, 38756−38766.

(29) Hoffman, B. M. *Acc. Chem. Res.* **2003**, *36*, 522−529.

(30) Hoffman, B. M. *Proc. Natl. Acad. Sci. U. S. A.* **2003**, *100*, 3575−3578.

(31) Yang, T. C.; Wolfe, M. D.; Neibergall, M. B.; Mekmouche, Y.; Lipscomb, J. D.; Hoffman, B. M. *J. Am. Chem. Soc.* **2003**, *125*, 7056−7066.

(32) Lipscomb, J. D.; Hoffman, B. M. *Structure* **2005**, *13*, 684−685.

(33) Muthukumaran, R. B.; Grzyska, P. K.; Hausinger, R. P.; McCracken, J. *Biochemistry* **2007**, *46*, 5951−5959.

(34) Nelson, M. J. *J. Biol. Chem.* **1987**, *262*, 12137−12142.

(35) Debus, R. J.; Campbell, K. A.; Gregor, W.; Li, Z.-L.; Burnap, R. L.; Britt, R. D. *Biochemistry* **2001**, *40*, 3690−3699.

(36) Hoogstraten, C. G.; Grant, C. V.; Horton, T. E.; DeRose, V. J.; Britt, R. D. *J. Am. Chem. Soc.* **2002**, *124*, 834−842.

(37) Schiemann, O.; Carmieli, R.; Goldfarb, D. *Appl. Magn. Reson.* **2007**, *31*, 543−552.

(38) Potapov, A.; Goldfarb, D. *Inorg. Chem.* **2008**, *47*, 10491−10498.

(39) McNaughton, R. L.; Reddi, A. R.; Clement, M.; Sharma, A.; Barnese, K.; Rosenfeld, L.; Gralla, E. B.; Valentine, J. S.; Culotta, V. C.; Hoffman, B. M. *Proc. Natl. Acad. Sci. U. S. A.* **2010**, *107*, 15335−15339.

(40) Kaminker, I.; Sushenko, A.; Potapov, A.; Daube, S.; Akabayov, B.; Sagi, I.; Goldfarb, D. *J. Am. Chem. Soc.* **2011**, *133*, 15514−15523.

(41) Sharma, A.; Gaidamakova, E. K.; Matrosova, V. Y.; Bennett, B.; Daly, M. J.; Hoffman, B. M. *Proc. Natl. Acad. Sci. U. S. A.* **2013**, *110*, 5945−5950.

(42) Hu, S.; Sharma, S. C.; Scouras, A. D.; Soudackov, A. V.; Carr, C. A. M.; Hammes-Schiffer, S.; Alber, T.; Klinman, J. K. *J. Am. Chem. Soc.* **2014**, *136*, 8157−8160.

(43) Solomon, E. I.; Zhou, J.; Neese, F.; Pavel, E. G. *Chem. Biol.* **1997**, *4*, 795−808.

(44) Newcomer, M. E.; Brash, A. R. *Protein Sci.* **2015**, *24*, 298−309.

(45) Yu, T.; Soudackov, A. V.; Hammes-Schiffer, S. *J. Phys. Chem. Lett.* **2016**, *7*, 3429−3433.

(46) Su, C.; Oliw, E. H. *J. Biol. Chem.* **1998**, *273*, 13072−13079.

(47) Newie, J.; Kasanmascheff, M.; Bennati, M.; Feussner, I. *Lipids* **2016**, *51*, 335−347.

(48) Lehnert, N.; Solomon, E. I. *J. Biol. Inorg. Chem.* **2003**, *8*, 294−305.

(49) Hirao, H.; Morokuma, K. *J. Phys. Chem. Lett.* **2010**, *1*, 901−906.

(50) Magnusson, O. T.; Reed, G. H.; Frey, P. A. *J. Am. Chem. Soc.* **1999**, *121*, 9764−9765.

(51) Coffino, A. R.; Peisach, J. *J. Magn. Reson., Ser. B* **1996**, *111*, 127−134.

(52) Reed, G. H.; Markham, G. D. In *Biological Magnetic Resonance*; Berliner, L. J., Reuben, J., Eds.; Plenum Press: New York, 1984; Vol. 6, pp 73−142.

(53) Gaffney, B. J.; Su, C.; Oliw, E. H. *Appl. Magn. Reson.* **2001**, *21*, 411−422.

(54) Wennman, A.; Oliw, E. H.; Karkehabadi, S.; Chen, Y. *J. Biol. Chem.* **2016**, *291*, 8130−8139.

(55) Horitani, M.; Byer, A. S.; Shisler, K. A.; Chandra, T.; Broderick, J. B.; Hoffman, B. M. *J. Am. Chem. Soc.* **2015**, *137*, 7111−7121.

(56) We note that, to our knowledge, there has never been an experiment prior to this that could have detected this "gossamer" of spin density surrounding a paramagenetic site.

(57) Hoffman, B. M.; Martinsen, J.; Venters, R. A. *J. Magn. Reson.* **1984**, *59*, 110−123.

(58) Hoffman, B. M.; Gurbiel, R. J.; Werst, M. M.; Sivaraja, M. In *Advanced EPR, Applications in Biology and Biochemistry*; Hoff, A. J., Ed.; Elsevier: Amsterdam, 1989; pp 541−591.

(59) DeRose, V. J.; Hoffman, B. M. In *Methods in Enzymology*; Sauer, K., Ed.; Academic Press: New York, 1995; Vol. 246, pp 554−589.

(60) Ruddat, V. C.; Mogul, R.; Chorny, I.; Chen, C.; Perrin, N.; Whitman, S.; Kenyon, V.; Jacobson, M. P.; Bernasconi, C. F.; Holman, T. R. *Biochemistry* 2004, 43, 13063−13071.

(61) Wu, F.; Gaffney, B. J. *Biochemistry* 2006, 45, 12510−12518.

(62) Chohany, L. E.; Bishop, K. A.; Camic, H.; Sup, S. J.; Findeis, P. M.; Clapp, C. H. *Bioorg. Chem.* 2011, 39, 94−100.

(63) Neau, D. B.; Bender, G.; Boeglin, W. E.; Bartlett, S. G.; Brash, A. R.; Newcomer, M. E. *J. Biol. Chem.* 2014, 289, 31905−31913.

(64) Collazo, L.; Klinman, J. K. *J. Biol. Chem.* 2016, 291, 9052−9059.

(65) Layfield, J. P.; Hammes-Schiffer, S. *Chem. Rev.* 2014, 114, 3466−3494.

(66) Soudackov, A. V.; Hammes-Schiffer, S. *J. Phys. Chem. Lett.* 2015, 5, 3274−3278.

(67) Marcus, R. A.; Sutin, N. *Biochim. Biophys. Acta, Rev. Bioenerg.* 1985, 811, 265−322.

(68) Gilbert, N. C.; Rui, Z.; Neau, D. B.; Waight, M. T.; Bartlett, S. G.; Boeglin, W. E.; Brash, A. R.; Newcomer, M. E. *FASEB J.* 2012, 26, 3222−3229.

(69) Kobe, M. J.; Neau, D. B.; Mitchell, C. E.; Bartlett, S. G.; Newcomer, M. E. *J. Biol. Chem.* 2014, 289, 8562−8569.

(70) These enzymes were heavily engineered, and the binding of substrate in these structures accompanied the loss of catalytically important metal ligands. Thus, the relevance of these ES models to catalysis remains unestablished.

(71) Sikorski, R. S.; Wang, L.; Markham, K. A.; Rajagopalan, P. T. R.; Benkovic, S. J.; Kohen, A. *J. Am. Chem. Soc.* 2004, 126, 4778−4779.

(72) Agarwal, P. K.; Billeter, S. R.; Rajagopalan, P. T. R.; Benkovic, S. J.; Hammes-Schiffer, S. *Proc. Natl. Acad. Sci. U. S. A.* 2002, 99, 2794−2799.

(73) Henzler-Wildman, K.; Kern, D. *Nature* 2007, 450, 964−972.

(74) Benkovic, S. J.; Hammes, G. G.; Hammes-Schiffer, S. *Biochemistry* 2008, 47, 3317−3321.

(75) Hatcher, E.; Soudackov, A. V.; Hammes-Schiffer, S. *J. Am. Chem. Soc.* 2004, 126, 5763−5775.

(76) Offenbacher, A. R.; Zhu, H.; Klinman, J. K. *Tetrahedron Lett.* 2016, 57, 4537−4540.

(77) Artimo, P.; Jonnalagedda, M.; Arnold, K.; Baratin, D.; Csardi, G.; de Castro, E.; Duvaud, S.; Flegel, V.; Fortier, A.; Gasteiger, E.; Grosdidier, A.; Hernandez, C.; Ioannidis, V.; Kuznetsov, D.; Liechti, R.; Moretti, S.; Mostaguir, K.; Redaschi, N.; Rossier, G.; Xenarios, I.; Stockinger, H. *Nucleic Acids Res.* 2012, 40, W597−W603.

(78) Riemer, J.; Hoepken, H. H.; Czerwinska, H.; Robinson, S. R.; Dringen, R. *Anal. Biochem.* 2004, 331, 370−375.

(79) Carr, C. A. M. University of California, Berkeley, 2011.

(80) Winn, M. D.; Ballard, C. C.; Cowtan, K. D.; Dodson, E. J.; Emsley, P.; Evans, P. R.; Keegan, R. M.; Krissinel, E. B.; Leslie, A. G. W.; McCoy, A.; McNicholas, S. J.; Murshudov, G. N.; Pannu, N. S.; Potterton, E. A.; Powell, H. R.; Read, R. J.; Vagin, A.; Wilson, K. S. *Acta Crystallogr., Sect. D: Biol. Crystallogr.* 2011, 67, 235−242.

(81) Leslie, A. G. W.; Powell, H. R. *Evolving Methods for Macromolecular Crystallography*; Springer: Netherlands, 2007.

(82) Evans, P. *Acta Crystallogr., Sect. D: Biol. Crystallogr.* 2006, 62, 72−82.

(83) Evans, P. R. *Acta Crystallogr., Sect. D: Biol. Crystallogr.* 2011, 67, 282−292.

(84) Zwart, P. H. *Acta Crystallogr., Sect. D: Biol. Crystallogr.* 2005, 61, 1437−1448.

(85) Dauter, Z. *Acta Crystallogr., Sect. D: Biol. Crystallogr.* 2006, 62, 1−11.

(86) McCoy, A. J.; Grosse-Kunstleve, R. W.; Adams, P. D.; Winn, M. D.; Storoni, L. C.; Read, R. J. *J. Appl. Crystallogr.* 2007, 40, 658−674.

(87) Emsley, P.; Cowtan, K. D. *Acta Crystallogr., Sect. D: Biol. Crystallogr.* 2004, 60, 2126−2132.

(88) Emsley, P.; Lohkamp, B.; Scott, W. G.; Cowtan, K. *Acta Crystallogr., Sect. D: Biol. Crystallogr.* 2010, 66, 486−501.

(89) Adams, P. D.; Afonine, P. V.; Bunkoczi, G.; Chen, V. B.; Davis, I. W.; Echols, N.; Headd, J. J.; Hung, L.-W.; Kapral, G. J.; Grosse-Kunstleve, R. W.; McCoy, A. J.; Moriarty, N. W.; Oeffner, R.; Read, R. J.; Richardson, D. C.; Richardson, J. S.; Terwilliger, T. C.; Zwart, P. H. *Acta Crystallogr., Sect. D: Biol. Crystallogr.* 2010, 66, 213−221.

(90) Chattopadhyay, A.; London, E. *Anal. Biochem.* 1984, 139, 408−412.

(91) Schowen, K. B.; Schowen, R. L. *Methods Enzymol.* 1982, 87, 551−606.

(92) Werst, M. M.; Davoust, C. E.; Hoffman, B. M. *J. Am. Chem. Soc.* 1991, 113, 1533−1538.

(93) Schweiger, A.; Jeschke, G. *Principles of Pulse Electron Paramagnetic Resonance*; Oxford University Press: Oxford, UK, 2001.

(94) Davoust, C. E.; Doan, P. E.; Hoffman, B. M. *J. Magn. Reson., Ser. A* 1996, 119, 38−44.

(95) Xu, W.; Lees, N.; Adedeji, D.; Wiesner, J.; Jomaa, H.; Hoffman, B. M.; Duin, E. *J. Am. Chem. Soc.* 2010, 132, 14509−14520.

(96) Doan, P. E.; Lees, N. S.; Shanmugam, M.; Hoffman, B. M. *Appl. Magn. Reson.* 2010, 37, 763−779.

(97) Phillips, J. C.; Braun, R.; Wang, W.; Gumbart, J.; Tajkhorshid, E.; Villa, E.; Chipot, C.; Skeel, R. D.; Kalé, L.; Schulten, K. *J. Comput. Chem.* 2005, 26, 1781−1802.

(98) Petrey, D.; Xiang, Z.; Tang, C. L.; Xie, L.; Gimpelev, M.; Mitros, T.; Soto, C. S.; Goldsmith-Fischman, S.; Kernytsky, A.; Schlessinger, A.; Koh, I. Y. Y.; Alexov, E.; Honig, B. *Proteins: Struct., Funct., Genet.* 2003, 53, 430−435.

(99) Xiang, Z.; Honig, B. *J. Mol. Biol.* 2001, 311, 421−430.

(100) Bashford, D.; Karplus, M. *Biochemistry* 1990, 29, 10219−10225.

(101) Gordon, J. C.; Myers, J. B.; Folta, T.; Shoja, V.; Heath, L. S.; Onufriev, A. *Nucleic Acids Res.* 2005, 33, W368−W371.

(102) *The PyMOL Molecular Graphics System*, version 6.2; Schrödinger, LLC: New York, 2014.

(103) Cornell, W. D.; Cieplak, P.; Bayly, C. I.; Gould, I. R.; Merz, K. M.; Ferguson, D. M.; Spellmeyer, D. C.; Fox, T.; Caldwell, J. W.; Kollman, P. A. *J. Am. Chem. Soc.* 1995, 117, 5179−5197.

(104) Cheatham, T. E., III; Cieplak, P.; Kollman, P. A. *J. Biomol. Struct. Dyn.* 1999, 16, 845−862.

(105) Pérez, A.; Marchán, I.; Svozil, D.; Sponer, J.; Cheatham, T. E., III; Laughton, C. A.; Orozco, M. *Biophys. J.* 2007, 92, 3817−3829.

(106) Hornak, V.; Abel, R.; Okur, A.; Strockbine, B.; Roitberg, A.; Simmerling, C. *Proteins: Struct., Funct., Genet.* 2006, 65, 712−725.

(107) Harshan, A. K.; Yu, T.; Soudackov, A. V.; Hammes-Schiffer, S. *J. Am. Chem. Soc.* 2015, 137, 13545−13555.

(108) Hay, P. J.; Wadt, W. R. *J. Chem. Phys.* 1985, 82, 270−283.

(109) Zhou, Z.; Khan, S. U. M. *J. Phys. Chem.* 1989, 93, 5292−5295.

(110) Jorgensen, W. L.; Chandrasekhar, J.; Madura, J. D.; Impey, R. W.; Klein, M. L. *J. Chem. Phys.* 1983, 79, 926−935.